arXiv:1511.08492v1 [cond-mat.quant-gas] 26 Nov 2015

Experimental observation of topological band gap opening in ultracold Fermi gases with two-dimensional spin-orbit coupling

Zengming Meng,[1,2] Lianghui Huang,[1,2] Peng Peng,[1] Donghao Li,[1] Liangchao Chen,[1] Yong Xu,[3] Chuanwei Zhang,[3] Pengjun Wang,[1,2] and Jing Zhang[1,4,*]

[1] *State Key Laboratory of Quantum Optics and Quantum Optics Devices, Institute of Opto-Electronics, Shanxi University, Taiyuan 030006, P.R.China*
[2] *Collaborative Innovation Center of Extreme Optics, Shanxi University, Taiyuan 030006, P.R.China*
[3] *Department of Physics, The University of Texas at Dallas, Richardson, Texas 75080-3021, USA*
[4] *Synergetic Innovation Center of Quantum Information and Quantum Physics, University of Science and Technology of China, Hefei, Anhui 230026, P. R. China*

Spin-orbit coupling (SOC) and Zeeman fields are crucial ingredients for many topological quantum matters. In this context, the recent experimental realization of synthetic SOC, both one-dimensional (1D) and two-dimensional (2D), opens a new avenue for exploring topological states with ultracold atoms. However, in 2D SOC (e.g., Rashba type), a perpendicular Zeeman field, which opens a band gap at the Dirac point and induces topological properties, has not been realized in experiments for ultracold atoms. Here we propose and realize a simple scheme for generating 2D SOC and a perpendicular Zeeman field simultaneously in ultracold Fermi gases by tuning the polarization of three Raman lasers that couple three hyperfine ground states of atoms. The resulting band gap opening at the Dirac point is probed using spin injection radio-frequency spectroscopy. Our observation may pave the way for exploring topological transport and topological superfluids with exotic Majorana and Weyl fermion excitations in ultracold atoms.

Spin-orbit coupling (SOC), the intrinsic interaction between a particle's spin and motion, plays an essential role for a variety of topological quantum materials, ranging from topological insulators of non-interacting electrons to topological superconductors with Majorana quasiparticles [1–3]. In these materials, a perpendicular (i.e., orthogonal to the SOC plane) Zeeman field is often crucially important for breaking the time-reversal symmetry and opening a topological band gap. For instance, such topological band gap opening can lead to the intrinsic anomalous Hall effects in spin-orbit coupled semiconductor materials [4, 5]. Another example is the 1D or 2D spin-orbit coupled s-wave superconductors/superfluids, which become topological and support exotic Majorana fermion (MF) excitations [6] in the presence of a large perpendicular Zeeman field [7–10]. In 3D, the same system also exhibits the long-sought Weyl fermion physics in the superconducting quasiparticle excitation spectrum [11–13]. Remarkably, some possible signatures of MFs have been experimentally observed recently in semiconductor/superconductor heterostructures [14–18] following the theoretical proposals, although unambiguous evidences are still lacked because of the strong disorder in solid state materials.

In this context, the recent experimental realization of synthetic SOC for cold atoms [19–26] provides a completely new and clean platform for exploring topological quantum materials. Early experiments only realized the 1D SOC (*i.e.*, an equal sum of Rashba [27] and Dresselhaus [28] coupling, $\propto k_x\sigma_y$) with a tunable Zeeman field using two counter-propagating Raman lasers [19–26]. Many theoretical proposals already existed that are capable of generating 2D SOC (*i.e.*, $\propto \alpha k_x\sigma_y + \beta k_y\sigma_x$), especially Rashba or Dresselhaus type [29–35]. Fermi gases with such 2D SOC possess many interesting physical properties [11, 36–38]. Recently, 2D SOC was experimentally realized in ultracold ^{40}K Fermi gases [39] using three Raman lasers, each of which dresses one atomic hyperfine ground state. The associated stable Dirac point on a 2D momentum plane was observed [39]. However, the observation of topological superfluids and the associated Majorana and Weyl fermions requires a perpendicular Zeeman field, which is lacked in the experiment, to break the Fermi doubling theorem by opening a band gap and induce topological phases [7–10].

In this paper, we theoretically propose and experimentally realize a simple scheme for generating 2D SOC and a perpendicular Zeeman field simultaneously. The same setup for generating 2D SOC in previous work [39] is used, in which three far-detuned Raman lasers couple three hyperfine ground states. We only change the polarization of the Raman lasers, which can create the perpendicular Zeeman field and open the band gap at the Dirac point. This scheme significantly simplifies the experimental requirement compared with existing theoretical proposals [40, 41], which need additional laser beams, complicated optical configuration, and controllable relative laser phases to create the perpendicular Zeeman field. We observe and characterize the topological band gap opening induced by the perpendicular Zeeman field using spin injection radio-frequency (rf) spectroscopy, which are in good agreement with our theoretical calculations. The realization of 2D SOC and a perpendicular Zeeman field simultaneously provides a powerful platform for designing new atomtronic devices and may pave the way for experimental observation of many exotic topological

quantum phenomena, such as intrinsic anomalous Hall effects [4, 5], and topological superfluids with exotic quasiparticle excitations (e.g., Majorana or Weyl fermions) [7–13] in ultracold atomic gases.

Results

Experimental setup and theoretical modelling: Consider ultracold ^{40}K Fermi gases with three relevant hyperfine states, within the $4^2S_{1/2}$ ground electronic manifold, $|1\rangle = |F = 9/2, m_F = 3/2\rangle$, $|2\rangle = |F = 9/2, m_F = 1/2\rangle$ and $|3\rangle = |F = 7/2, m_F = 1/2\rangle$, where (F, m_F) are the quantum numbers for hyperfine ground states as shown in Fig. 1a. A homogeneous bias magnetic field $B_0 = 121.4$ G along the z axis (the gravity direction) produces a Zeeman shift to isolate these three hyperfine states from others in the Raman transitions, as shown in Fig. 1a. We can neglect other hyperfine states and treat this system as one with three ground states. Three far-detuned Raman lasers propagating on the xy plane couple these three ground states to the electronically excited states. For ^{40}K, the excited states include a fine-structure doublet $4^2P_{1/2}$ (D_1 line) and $4^2P_{3/2}$ (D_2 line) with fine structure splitting of ~ 3.4 nm. Each of two D-line components has additional hyperfine structures. For the far-detuned lasers, the excited states can be adiabatically eliminated, and the Hamiltonian is written as $H = p_z^2/(2m) + H_{xy}$ with

$$H_{xy} = \sum_{j=1}^{3}\left(\frac{(\mathbf{p}-\mathbf{k}_j)^2}{2m} + \delta_j\right)|j\rangle\langle j| - \sum_{j'\neq j}\frac{\Omega_{jj'}}{2}|j\rangle\langle j'| \quad (1)$$

under the hyperfine ground state basis $\{|j\rangle, j = 1, 2, 3\}$. Here $\mathbf{p} = p_x\mathbf{e}_x + p_y\mathbf{e}_y$ denotes the momentum of atoms in the xy plane, δ_1 is set as zero (energy reference) for simplification, δ_2 (δ_3) corresponds to the two-photon Raman detuning between Raman lasers 1 and 2 (1 and 3). $\mathbf{k}_1 = k_r\mathbf{e}_y$, $\mathbf{k}_2 = -k_r\mathbf{e}_y$, and $\mathbf{k}_3 = k_r\mathbf{e}_x$ are the photon momenta of three Raman lasers with the single-photon recoil momentum $k_r = 2\pi\hbar/\lambda$. Three $\Omega_{jj'} = \Omega^*_{j'j}$ describe the Raman coupling strength between hyperfine ground states $|j\rangle \leftrightarrow |j'\rangle$. The single-photon recoil momentum k_r and recoil energy $E_r = k_r^2/2m$ are taken as natural momentum and energy units.

The non-diagonal terms $\Omega_{jj'}$ in Hamiltonian (1) describe the coupling of three hyperfine ground states through Raman lasers. The eigenstates of such atom-laser interaction part of the Hamiltonian (1) contain two degenerate dark states and one bright state separated by an energy gap [42]. Denote two degenerate dark states as the pseudo-spin states, the 3×3 Hamiltonian (1) can be projected to the dark state subspace, leading to an effective spin-half Hamiltonian with 2D SOC and effective Zeeman fields. In previous experiments as well as existing theoretical proposals, $\Omega_{jj'}$ are taken as real numbers (*i.e.*, $\Omega_{jj'} = \Omega_{j'j}$) [43], yielding an effective 2D spin-half Hamiltonian

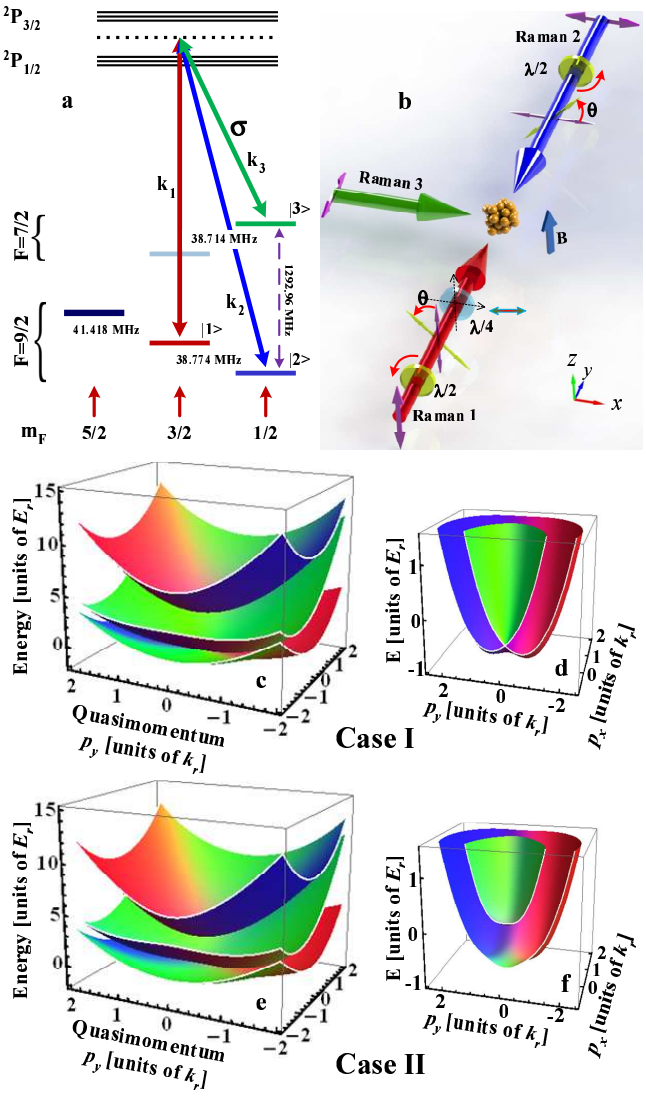

FIG. 1: **Scheme of the atom-light interaction configuration for generating 2D synthetic SOC and an effective perpendicular Zeeman field simultaneously.** (**a**) Schematic of energy levels of ^{40}K for creating 2D SOC and an effective perpendicular Zeeman field. Each of the three Raman lasers dresses one hyperfine ground state. (**b**) The experimental geometry and laser configuration. The Raman lasers 1 and 2 counter-propagate along the y axis and the Raman laser 3 propagates along the x axis. They are initially prepared with the linear polarization along the z, x and y directions, respectively. Then the Raman lasers 1 and 2 pass through a $\lambda/2$ waveplate, which rotates their linear polarizations by the same angle θ synchronously. Cases I and II correspond to without and with the $\lambda/4$ waveplate after the $\lambda/2$ waveplate for the Raman laser 1. (**c**) and (**e**) are energy-momentum dispersions without (case I) and with (case II) effective perpendicular Zeeman fields. (**d**) and (**f**) enlarge the low energy parts of (**c**) and (**e**), which show the Dirac point (**d**) and the band gap opening (**f**). Here, $\delta_2 = 0$, $\delta_3 = -0.5E_r$, $-\Omega_{12} = 2\Omega_{13} = 2\Omega_{23} = 3.5E_r$, and $\theta = 45^\circ$.

$$H_{eff} = \frac{\mathbf{p}^2}{2m} + H_{SOC} + V_I, \tag{2}$$

where the 2D SOC $H_{SOC} = -\alpha p_y \sigma_x + (\beta_x p_x - \beta_y p_y)\,\sigma_y$ and the in-plane Zeeman field $V_I = V_x\sigma_x + V_y\sigma_y$ in the xy plane. α, β_x, β_y, V_x, and V_y are parameters determined by the experimental parameters $\mathbf{k}_j$, δ_j, and $\Omega_{jj'}$ [42]. Pauli matrices σ_i are defined on the dark state pseudo-spin basis. Clearly, the in-plane Zeeman field V_I shifts the Dirac cone at $\mathbf{p} = \mathbf{0}$ to another position in the momentum space, but cannot open a band gap at the Dirac point. A perpendicular Zeeman field of the form $V_z\sigma_z$ is needed to open the band gap for the realization of topological quantum materials.

Realization of a perpendicular Zeeman field: Now we show how to implement an effective perpendicular Zeeman field by generating an imaginary part of the Raman coupling strength Ω_{12} through simply manipulating the polarization of three Raman lasers. In the experiment (Fig. 1), the Raman laser 3 couples the ground state $|3\rangle$ and propagates along the x axis, whose polarization is fixed and linearly polarized along the y direction $\overrightarrow{E}_3 = A_3\hat{\mathbf{e}}_\perp$, corresponding to the σ polarization (relative to the quantization axis $\mathbf{z}$ defined by the magnetic field). The Raman laser 2 couples the ground state $|2\rangle$ and propagates along the y axis. The linear polarization of the Raman laser 2 is initially prepared along the x direction (σ polarization) and rotated on the xz plane by a $\lambda/2$ waveplate, yielding $\overrightarrow{E}_2 = A_2(\cos\theta\hat{\mathbf{e}}_\perp + \sin\theta\hat{\mathbf{e}}_\parallel)$, where $\hat{\mathbf{e}}_\perp$ and $\hat{\mathbf{e}}_\parallel$ components correspond to σ and π polarizations. The Raman laser 1 couples the ground state $|1\rangle$ and propagates along the y axis. The linear polarization of the Raman laser 1 is prepared along the z direction (π polarization) and also rotated by an angle θ using a $\lambda/2$ waveplate ($\overrightarrow{E}_1 = A_1(\cos\theta\hat{\mathbf{e}}_\parallel + \sin\theta\hat{\mathbf{e}}_\perp)$) to keep orthogonal with the polarization of the Raman laser 2.

The linear polarization of the Raman laser 1 can be further tuned to elliptical polarization by inserting a $\lambda/4$ waveplate with the optical axis aligned along the $\mathbf{z}$ direction after the $\lambda/2$ waveplate. Therefore we can consider two different cases for the polarization of the Raman laser 1 for comparison: I) linear polarization without the $\lambda/4$ waveplate; II) elliptical polarization with the $\lambda/4$ waveplate.

Case I: Because the difference $\Delta m = 0$ between the hyperfine Zeeman states $|2\rangle$ and $|3\rangle$, only σ-σ polarization can drive the Raman transition between $|2\rangle$ and $|3\rangle$, yielding the Raman coupling strength $\Omega_{23}^I = \cos\theta A_2 A_3 r_{23} = \cos\theta\Omega_{23}$. Hereafter we denote $\Omega_{jj'}$ as the Raman coupling strength before the $\lambda/2$ and $\lambda/4$ waveplates. Similarly, the difference $\Delta m = 1$ between states $|1\rangle$ and $|3\rangle$ allows only π-σ polarization driven transition, yielding $\Omega_{13}^I = \cos\theta A_1 A_3 r_{13} = \cos\theta\Omega_{13}$. While $\Omega_{12}^I = A_1 A_2 r_{12}(\cos^2\theta + \sin^2\theta) = \Omega_{12}$ ($\Delta m = 1$ between states $|1\rangle$ and $|2\rangle$), which is unchanged when the linear polarizations of two Raman lasers keep orthogonal. We see such rotations keep the Hamiltonian (1) real, similar as that without the $\lambda/2$ waveplate (i.e., $\theta = 0$), therefore only shift the Dirac point position and cannot open a band gap (Fig. 1c and 1d).

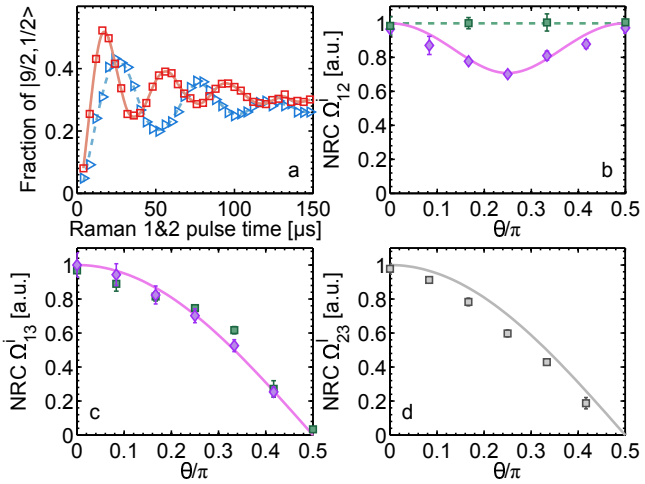

FIG. 2: **Measure the Raman coupling strength by Rabi oscillations between two hyperfine ground states.** (**a**) The population in $|2\rangle$ as a function of duration time of the Raman lasers 1 and 2 pulse. The red squares and blue trangles correspond to the polarization rotation angles $\theta = 0^o$ and 45^o respectively. The solid and dashed lines are fitting curves. (**b**) and (**c**) Plot of the Raman coupling strengths Ω_{12}^i and Ω_{13}^i versus θ. The green squares and purple diamonds correspond to cases I and II respectively. NRC represents normalized Raman coupling. (**d**) Plot of Ω_{23}^I versus θ. The solid and dashed lines in (**b-d**) are theoretical curves.

Case II: The $\lambda/4$ waveplate inserted after the $\lambda/2$ waveplate for the Raman laser 1 changes the linear polarization to the elliptical polarization with $\overrightarrow{E}_1 = A_1(\cos\theta\hat{\mathbf{e}}_\parallel + i\sin\theta\hat{\mathbf{e}}_\perp)$. The resulting Raman coupling strengths $\Omega_{13}^{II} = \cos\theta\Omega_{13}$ and $\Omega_{23}^{II} = \cos\theta\Omega_{23}$ are the same as the case I because of the same parallel polarization component. While $\Omega_{12}^{II} = A_1 A_2 r_{12}(\cos^2\theta + i\sin^2\theta) = \Omega_{12}(\cos^2\theta + i\sin^2\theta)$, yielding an imaginary part $H_Z = -i\frac{\Omega_{12}\sin^2\theta}{2}|1\rangle\langle 2| + H.c$ in the Hamiltonian (1), which could not be gauged out by varying the phase of the wavefunction for each hyperfine ground state. This term opens a band gap at the Dirac point as shown in Fig. 1e and 1f and is equivalent to an effective perpendicular Zeeman field. In fact, in the degenerate dark state pseudo-spin basis, this term gives $V_z\sigma_z$, the perpendicular Zeeman field [42]. The energy gap at the Dirac point can be controlled precisely by adjusting the rotation angle θ. Note H_Z has the same form as that in previous theoretical proposal [41], where two additional laser beams with frequencies different from the original three Raman laser are used and their relative phases need be controlled in order to introduce the imaginary part. Here we only

change the polarization of three original lasers and the elliptical polarization introduces the imaginary part H_Z. Therefore our scheme is much simpler and more robust than previous theoretical schemes.

We measure the Raman coupling strength one by one using the Rabi oscillation between two hyperfine ground states [24]. For the measurement of Ω_{12}^i ($i = I$ or II), all atoms are initially prepared in the $|1\rangle$ state. The two-photon Raman detuning between Raman lasers 1 and 2 is set as $\delta_2 = -(\mathbf{k}_1 - \mathbf{k}_2)^2/2m$ so that the $p_y = 0$ momentum component of state $|1\rangle$ is at resonance with the $p_y = 2k_r$ component of state $|2\rangle$. We then apply a Raman pulse (without the Raman laser 3) to the system and measure the spin population for different duration times of the Raman pulse. We determine the value of the Raman coupling strength by fitting the measurement of the Rabi oscillation as shown in Fig. 2a. We obtain Ω_{12}^i for cases I and II respectively as the function of the rotation angle θ as shown in Fig. 2b. For case I, Ω_{12}^I keeps unchanged for different θ. In case II, we measure the absolute value (or magnitude) $\sqrt{\cos^4\theta + \sin^4\theta}$ (as shown in Fig. 2b) of Ω_{12}^{II} because Ω_{12}^{II} is a complex number. Applying the same method, we measure Ω_{13}^i and Ω_{23}^i for two cases. Ω_{13}^i and Ω_{23}^i show the same cosine function for different θ as shown in Figs. 2c and 2d, which are in good agreement with the theoretical prediction.

Observation of band gap opening: We measure the energy-momentum dispersions of three dressed states with 2D SOC and a perpendicular Zeeman field by spin injection rf spectroscopy, which uses rf field to drive atoms from a free spin-polarized state at $|9/2, 5/2\rangle$ into an empty 2D SOC system. Since rf field does not transfer momentum to the atoms, spin injection occurs when the frequency of the rf matches the energy difference between the initial and final states (see Methods).

Fig. 3 shows the momentum-resolved spin-injection spectra for case I (without $\lambda/4$ waveplate) and case II (with $\lambda/4$ waveplate). Other experimental parameters are the same for two cases. When the wavelength of the Raman lasers is tuned to 768.85 nm between the D_1 line and D_2 line, two lower energy dispersions touch at a Dirac point for case I, as shown in Figs. 3(a1)-(a5). With the $\lambda/4$ waveplate (case II), the energy gap at the Dirac point is opened, which is induced by the effective perpendicular Zeeman field, as shown in Fig. 3(b1)-(b5). We also perform numerical calculations for the energy spectra of the Hamiltonian (1) and the effective Hamiltonian (2) with corresponding experimental parameters. They show good agreement with the experimental data. Note that the eigenenergy of the effective 2×2 spin Hamiltonian (2) deviates from the exact 3×3 Hamiltonian (1) for momentum away from the Dirac points.

Fig. 4 shows the energy gap at the Dirac point and the corresponding Dirac point positions in the momentum space as a function of the polarization rotation angle θ. We see the band gap increases with the angle

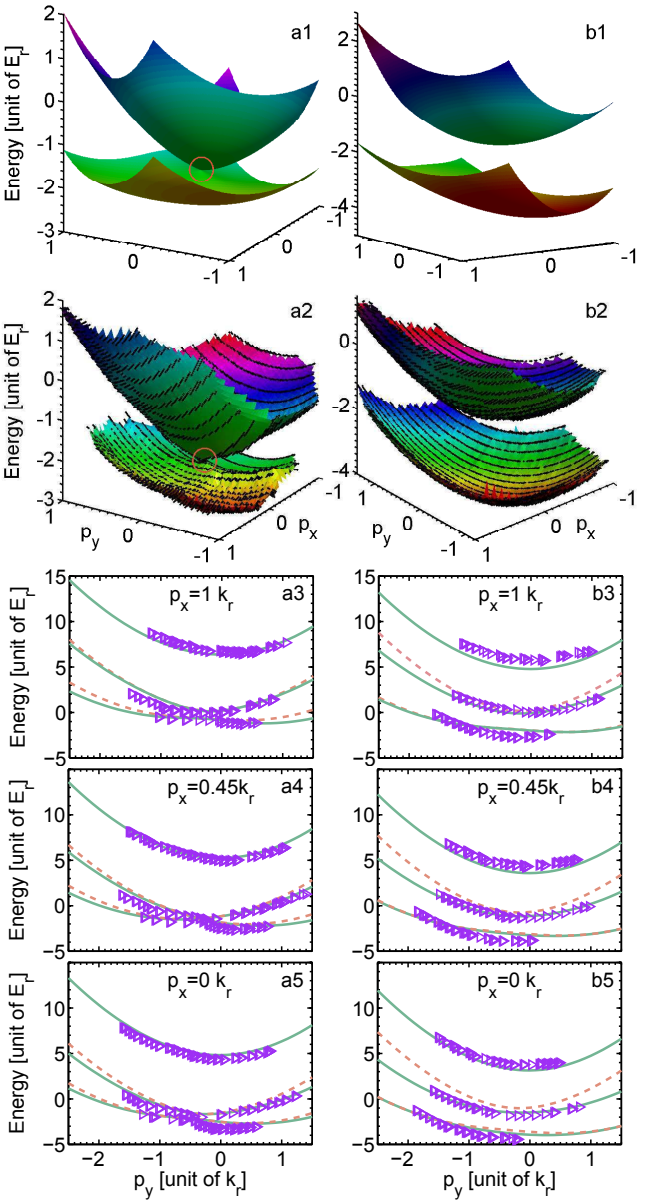

FIG. 3: **The energy dispersions of dressed atoms measured by rf spin-injection spectroscopy.** Columns **(a1)-(a5)** and **(b1)-(b5)** correspond to the energy-momentum dispersions of 2D SOC without (case I) and with (case II) effective perpendicular Zeeman field, respectively. The experimental parameters are $\Omega_{12} = -4.97E_r$, $\Omega_{13} = 5.46E_r$, $\Omega_{23} = 6.46E_r$, $\delta_2 = -5E_r$, $\delta_3 = -1.8E_r$ and $\theta = 45^o$. **(a1)** and **(b1)** are theoretical results calculated using the Hamiltonian (1) with the experimental parameters. **(a2)** and **(b2)** are experimental results measured by rf spin-injection spectroscopy. The black dots represent the expermental data. The yellow circles in **(a1)** and **(a2)** indicate the Dirac points. In both rows, we only show the lowest two bands for better visulization of the Dirac points and the band gap opening. **(a3)-(a5)** The cross-section drawings of **(a1)** and **(a2)** in the energy-p_y coordinates for different quasimomentum p_x. Triangles are from experimental data. Solid and dashed lines are from theoretical calculations using the full (Eq. 1) and effective (Eq. 2) Hamiltonians, respectively. **(b3)-(b5)**, The cross-section drawings of (b1) and (b2).

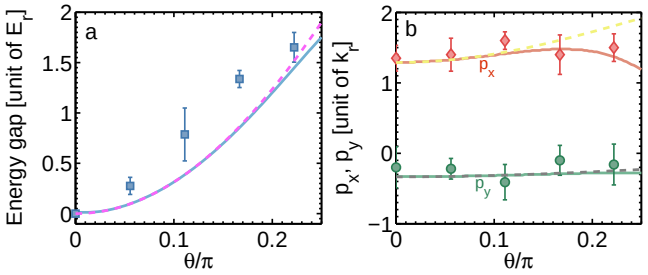

FIG. 4: **Tunable band gap at the Dirac point induced by the perpendicular Zeeman field**. The band gap (a) and the position of the Dirac point (b) are plotted as the function of the polarization rotation angle θ**.** In both figures, the squares and diamonds represent experimental data. The solid and dashed lines represent theoretical calculations using the 3×3 Hamiltonian (1) and the spin-half effective Hamiltonian (2) respectively. The experimental parameters are the same as Fig. 3.

θ, while the positons of the Dirac points only change slightly, demonstrating the tunability of the topological band gaps through varying the polarization of the Raman laser. The measured single particle band gaps do not exactly agree with the theoretical calculations from the Hamiltonian (1) and the effective Hamiltonian (2), which may be attributed to, for instance, the finite energy resolution of rf spectrum and the corresponding finite momentum width, the uncertainty in the Gaussian fit process to locate the maximum of the measured atomic density, and the stability of the magnetic field, etc.

Discussion

By varying the Raman laser intensities in experiments, the positions of the Dirac points, the form of the 2D SOC, and the associated in-plane Zeeman field can all be tuned. Together with the tunable perpendicular Zeeman field at the Dirac points, our system provides a potential platform for exploring various SOC related transport phenenoma for non-interacting atoms and superfluid physics for Cooper pairs. For instance, the coexistence of 2D SOC and the perpendicular Zeeman field yields non-zero Berry curvature, which leads to an anomalous velocity for atoms [4, 5]. The resulting anomalous Hall effects may be observed in a non-interacting Fermi gas [40]. The generated perpendicular Zeeman field is at the order of recoil energy E_r, which is large enough for realizing topological superfluids [7–10] and associated Majorana and Weyl fermions. The generated Zeeman field contains both in-plane and perpendicular components, which make the single particle band structure highly asymmetric, leading to the possibility of observing the long-sought Fulde-Ferrell-Larkin-Ovchinnikov superfluid phases with finite momentum pairing [44–46]. In particular, in the two-body physics level, such system could host a dimer bound state with finite center-of-mass mechanical momentum, which may be measured in the momentum distribution [47].

In summary, we have realized a simple scheme for generating two-dimensional spin-orbit coupling and a perpendicular Zeeman field simultaneously for ultracold fermionic atoms. The topological energy gap at the Dirac point can be opened and controlled precisely by the effective perpendicular Zeeman field. Our study should pave the way for exploring various interesting topological and other exotic superfluid phenomena arising from the s-wave scattering interaction.

Methods

Experimental procedure: A degenerate Fermi gas ^{40}K of 2×10^6 is prepared at the free reservoir hyperfine state $|9/2,5/2\rangle$ in a crossed optical dipole trap. We ramp the homogeneous bias magnetic field to the value $B_0 =$ 121.4 G, and then apply three Raman lasers with the wavelength 768.85 nm (between the D_1 line and D_2 line) in 60 ms from zero to its final value. Subsequently, a Gaussian shape pulse of the rf field is applied for 450 μs to drive atoms from the initial reservoir state $|9/2,5/2\rangle$ to the final empty state with 2D SOC. At last, the Raman lasers, the optical trap and the bias magnetic field are switched off abruptly, and atoms freely expand for 12 ms with a magnetic field gradient applied along the x axis. Absorption image is taken along the z direction. We use a Gaussian fit to locate the maximum of the measured atomic density as a function of the momentum and the rf frequency from the absorption image, from which we can obtain the energy band structure. In addition to the energy dispersions with 2D SOC, rf spectroscopy can measure the weight of the $|1\rangle$ state.

Effective band gap: The effective 2×2 spin Hamiltonian (2) is obtained by projecting the effective 3×3 atom-laser interaction Hamiltonian (mainly the non-diagonal part of Hamiltonian (1)) into its two degenerate dark eigenstate space (see supplementary information [42]). In case II, The gap at the Dirac points generated by perpendicular Zeeman field can be written as

$$\Delta = \sin^2\theta\left[\Omega_{12}^{-2}+\cos^2\theta\left(\Omega_{13}^{-2}+\Omega_{23}^{-2}\right)\right]^{-1/2}. \quad (3)$$

Clearly, the gap disappears for $\theta = 0$ (i.e., without the $\lambda/2$ waveplate) and can be continuously tuned by varying the polarization angle θ.

* Correspondence and requests for materials should be addressed to J.Z. (email: jzhang74@sxu.edu.cn, jzhang74@yahoo.com).

[1] Hasan, M. Z. & Kane, C. L. Topological insulators. *Rev. Mod. Phys.* **82**, 3045-3068 (2010).
[2] Qi, X.-L. & Zhang, S.-C. Topological insulators and superconductors. *Rev. Mod. Phys.* **83**, 1057-1110 (2011).
[3] Moore, J. E. The birth of topological insulators. *Nature* **464**, 194-198 (2010).

[4] Nagaosa, N., Sinova, J., Onoda, S., MacDonald, A.H. & Ong, N.P. Anomalous Hall effect. *Rev. Mod. Phys.* **82**, 1539-1592 (2010).

[5] Xiao, D., Chang, M.-C. & Niu, Q. Berry phases effects on electronic properties. *Rev. Mod. Phys.* **82**, 1959-2007 (2010).

[6] Wilczek, F. Majorana returns. *Nat. Phys.* 5, 614-618 (2009).

[7] Zhang, C., Tewari, S., Lutchyn, R. M. & Das Sarma S. $p_x + ip_y$ superfluid from s-wave interactions of fermionic cold atoms. *Phys. Rev. Lett.* **101**, 160401 (2008).

[8] Sau, J. D., Lutchyn, R. M., Tewari, S. & Das Sarma, S. Generic new platform for topological quantum computation using semiconductor heterostructures. *Phys. Rev. Lett.* **104**, 040502 (2010).

[9] Lutchyn, R. M., Sau, J. D. & Das Sarma, S. Majorana Fermions and a topological phase transition in semiconductor-superconductor heterostructures. *Phys. Rev. Lett.* **105**, 077001 (2010).

[10] Oreg, Y., Refael, G. & von Oppen, F. Helical liquids and Majorana bound states in quantum wires. *Phys. Rev. Lett.* **105**, 177002 (2010).

[11] Gong, M., Tewari, S. & Zhang, C. BCS-BEC crossover and topological phase transition in 3D spin-orbit coupled degenerate Fermi gases. *Phys. Rev. Lett.* **107**, 195303 (2011).

[12] Seo, K., Han, L. & Sá de Melo, C. A. R. Emergence of Majorana and Dirac particles in ultracold fermions via tunable interactions, spin-orbit effects, and Zeeman fields. *Phys. Rev. Lett.* **109**, 105303 (2012).

[13] Xu, Y., Chu, R. & Zhang, C. Anisotropic Weyl fermions from quasiparticle excitation spectrum of a 3D Fulde-Ferrell superfluid. *Phys. Rev. Lett.* **112**, 136402 (2014).

[14] Mourik, V., Zuo, K., Frolov, S. M., Plissard, S. R., Bakkers, E. P. A. M. & Kouwenhoven, L. P. Signatures of Majorana Fermions in hybrid superconductor-semiconductor nanowire devices. *Science* **336**, 1003-1007 (2012).

[15] Deng, M. T., Yu, C. L., Huang, G. Y., Larsson, M., Caroff, P. & Xu, H. Q. Anomalous zero-bias conductance peak in a Nb–InSb nanowire–Nb hybrid device. *Nano Lett.* **12**, 6414-6419 (2012).

[16] Das, A., Ronen, Y., Most, Y., Oreg, Y., Heiblum, M. & Shtrikman, H. Zero-bias peaks and splitting in an Al–InAs nanowire topological superconductor as a signature of Majorana fermions. *Nat. Phys.* **8**, 887-895 (2012).

[17] Rokhinson, L. P., Liu, X. & Furdyna J. K. The fractional a.c. Josephson effect in a semiconductor-superconductor nanowire as a signature of Majorana particles. *Nat. Phys.* **8**, 795-799 (2012).

[18] Nadj-Perge, S., Drozdov, I. K., Li, J., Chen, H., Jeon, S., Seo, J., MacDonald, A. H., Andrei Bernevig, B. & Yazdani, A. Observation of Majorana fermions in ferromagnetic atomic chains on a superconductor. *Science* **346**, 602-607 (2014).

[19] Lin, Y.-J., Jiménez-García, K. & Spielman, I. B. Spin-orbit-coupled Bose-Einstein condensates. *Nature* **471**, 83-86 (2011).

[20] Fu, Z., Wang, P., Chai, S., Huang, L. & Zhang, J. Bose-Einstein condensate in a light-induced vector gauge potential using the 1064 nm optical dipole trap lasers. *Phys. Rev. A* **84**, 043609 (2011).

[21] Zhang, J.-Y. *et al.* Collective dipole oscillations of a spin-orbit coupled Bose-Einstein condensate. *Phys. Rev. Lett.* **109**, 115301 (2012).

[22] Qu, C., Hamner, C., Gong, M., Zhang, C. & Engels, P. Observation of Zitterbewegung in a spin-orbit coupled Bose-Einstein condensates. *Phys. Rev. A* **88**, 021604(R) (2013)

[23] Olson, A. J., Wang, S. -J., Niffenegger, R. J., Li, C. -H., Greene, C. H. & Chen, Y. P. Tunable Laudan-Zener transitions in a spin-orbit-coupled Bose-Einstein condesate. *Phys. Rev. A* **90**, 013616 (2014).

[24] Wang, P., Yu, Z., Fu, Z., Miao, J., Huang, L., Chai, S., Zhai, H. & Zhang, J. Spin-orbit coupled degenerate Fermi gases. *Phys. Rev. Lett.* **109**, 095301 (2012).

[25] Cheuk, L. W. *et al.* Spin-injection spectroscopy of a spin-orbit coupled Fermi gas. *Phys. Rev. Lett.* **109**, 095302 (2012).

[26] Williams, R. A., Beeler, M. C., LeBlanc, L. J. & Spielman I. B. Raman-induced interactions in a single-component Fermi gas near an s-wave Feshbach resonance. *Phys. Rev. Lett.* **111**, 095301 (2013).

[27] Rashba, E. I. Properties of semiconductors with an extremum loop I: Cyclotron and combinational resonance in a magnetic field perpendicular to the plane of the loop. *Sov. Phys. Sol. St.* **2**, 1224-1238 (1960).

[28] Dresselhaus, G. Spin-orbit coupling effects in zinc blende structures. *Phys. Rev.* **100**, 580-586 (1955).

[29] Unanyan, R. G., Shore, B. W. & Bergmann, K. Laser-driven population transfer in four-level atoms: Consequences of non-abelian geometrical adiabatic phase factors. *Phys. Rev. A* **59**, 2910-2919 (1999).

[30] Ruseckas, J., Juzeliūnas, G., Öhberg, P. & Fleischhauer, M. Non-abelian gauge potentials for ultracold atoms with degenerate dark states. *Phys. Rev. Lett.* **95**, 010404 (2005).

[31] Campbell, D. L., Juzeliūnas, G. & Spielman, I. B. Realistic Rashba and Dresselhaus spin-orbit coupling for neutral atoms. *Phys. Rev. A* **84**, 025602 (2011).

[32] Xu, Z. F., You, L. & Ueda, M. Atomic spin-orbit coupling synthesized with magnetic-field-gradient pulses. *Phys. Rev. A* **87**, 063634 (2013).

[33] Anderson, B. M., Spielman, I. B. & Juzeliūnas, G. Magnetically generated spin-orbit coupling for ultracold atoms. *Phys. Rev. Lett.* **111**, 125301 (2013).

[34] Zhang, Y., Mao, L. & Zhang, C. Mean-field dynamics of spin-orbit coupled Bose-Einstein condensates. *Phys. Rev. Lett.* **108**, 035302 (2012).

[35] Campbell, D. L. & Spielman, I. B. Rashba realization: Raman with RF. arXiv:1511.01588.

[36] Vyasanakere, J. P. & Shenoy, V. B. Bound states of two spin-$\frac{1}{2}$ fermions in a synthetic non-Abelian gauge field. *Phys. Rev. B* **83**, 094515 (2011).

[37] Hu, H., Jiang, L., Liu, X. -J. & Han, P. Probing anisotropic superfluidity in atomic Fermi gases with Rashba spin-orbit coupling. *Phys. Rev. Lett.* **107**, 195304 (2011).

[38] Yu, Z. -Q. & Zhai, H. Spin-orbit coupled Fermi gases across a Feshbach resonance. *Phys. Rev. Lett.* **107**, 195305 (2011).

[39] Huang, L., Meng, Z., Wang, P., Peng, P., Zhang, S.-L., Chen, L., Li, D., Zhou, Q. & Zhang, J. Experimental realization of a two-dimensional synthetic spin-orbit coupling in ultracold Fermi gases. arXiv:1506.02861.

[40] Zhang, C. Spin-orbit coupling and perpendicular Zeeman field for fermionic cold atoms: Observation of the intrin-

sic anomalous Hall effect. *Phys. Rev. A* **82**, 021607(R) (2010).
[41] Zhu, S. -L., Shao, L. -B., Wang, Z. D. & Duan, L. -M. Probing non-Abelian statistics of Majorana Fermions in ultracold atomic superfluid. *Phys. Rev. Lett.* **106**, 100404 (2011).
[42] See the supplementary materials.
[43] Note that although different constant phases can be introduced for each Raman laser, which make all $\Omega_{jj'}$ complex, such phases can be easily gauged out by absorbing the phases into the definition of each hyperfine state wavefunction, yielding real $\Omega_{jj'}$.
[44] Zheng, Z., Gong, M., Zhou, X., Zhang, C. & Guo, G.-C. Route to observable Fulde-Ferrell-Larkin-Ovchinnikov phases in 3D spin-orbitcoupled degenerate Fermi gases. *Phys. Rev. A* **87**, 031602(R) (2013).
[45] Qu, C., Zheng, Z., Gong, M., Xu, Y., Mao, L., Zou, X., Guo, G.-C. & Zhang, C. Topological superfluids with finite-momentum pairing and Majorana fermions. *Nat. Commun.* **4**, 2710 (2013).
[46] Zhang, W. & Yi, W. Topological Fulde–Ferrell–Larkin–Ovchinnikov states in spin-orbit coupled Fermi gases. *Nat. Commun.* **4**, 2711 (2013).
[47] Dong, L., Jiang, L., Hu, H. & Pu, H. Finite-momentum dimer bound state in spin-orbit coupled Fermi gas. *Phys. Rev. A* **87**, 043616 (2013).

Acknowledgements: This research is supported by the National Basic Research Program of China (Grant No. 2011CB921601), NSFC (Grant No. 11234008, 11361161002, 11222430) and the program for Sanjin Scholars of Shanxi Province. Y.X. and C.Z are supported by ARO (W911NF-12-1-0334), AFOSR (FA9550-13-1-0045), and NSF (PHY-1505496).

Author contributions: Z.M., L.H., P.P., D.L., L.C., P.W. and J.Z. performed experiments. Y.X., C.Z., L.H., P.W. and J.Z. contributed to the theoretical modeling and explanation of the experimental data. C.Z. and J.Z. wrote the paper. Everybody discussed the results and commented on the manuscript. J.Z. supervised the project.

Competing financial interests

The authors declare no competing financial interests.

Supplementary Information

In the supplementary material, we derive the effective 2×2 spin Hamiltonian (Eq. (2) in the main text) from the full 3×3 Hamiltonian (Eq. 1 in the main text).

We write the Hamiltonian in Eq.(1) in the main text as the dimensionless one with the energy unit E_r and the momentum unit k_r,

$$\tilde{H}_{xy}=\begin{pmatrix}(\mathbf{p}-\mathbf{k}_1)^2 & -\frac{\bar{\Omega}_{12}^i}{2}-i\frac{\Gamma_{12}^i}{2} & -\frac{\Omega_{13}^i}{2}\\ -\frac{\Omega_{12}^i}{2}+i\frac{\Gamma_{12}}{2} & (\mathbf{p}-\mathbf{k}_2)^2+\delta_2 & -\frac{\Omega_{23}^i}{2}\\ -\frac{\Omega_{13}^i}{2} & -\frac{\Omega_{23}^i}{2} & (\mathbf{p}-\mathbf{k}_3)^2+\delta_3\end{pmatrix}. \tag{S1}$$

where $i=I$ or II for case I or II. $\bar{\Omega}_{12}^i$ and Γ_{12}^i are the real and imaginary parts of Ω_{12}^i. $\bar{\Omega}_{12}^I=\Omega_{12}$, $\bar{\Omega}_{12}^{II}=\Omega_{12}\cos^2\theta$, $\Gamma_{12}^I=0$, $\Gamma_{12}^{II}=\Omega_{12}\sin^2\theta$. Other parameters are the same as that in the main text. To obtain the degenerate dark states in the adiabatic approximation, we transfer the Hamiltonian back to the original position-dependent space

$$\tilde{H}_{xy}=\mathbf{p}^2+\tilde{H}_1+\tilde{H}_2+\tilde{H}_Z, \tag{S2}$$

where

$$\tilde{H}_1=\begin{pmatrix}-\bar{\Omega}_{12}^i\Omega_{13}^i/(2\Omega_{23}^i) & -\frac{\bar{\Omega}_{12}^i}{2}e^{-2iy} & -\frac{\Omega_{13}^i}{2}e^{i(x-y)}\\ -\frac{\bar{\Omega}_{12}^i}{2}e^{2iy} & -\bar{\Omega}_{12}^i\Omega_{23}^i/(2\Omega_{13}^i) & -\frac{\Omega_{23}^i}{2}e^{i(x+y)}\\ -\frac{\Omega_{13}^i}{2}e^{i(-x+y)} & -\frac{\Omega_{23}^i}{2}e^{-i(x+y)} & -\Omega_{13}^i\Omega_{23}^i/(2\bar{\Omega}_{12}^i)\end{pmatrix}, \tag{S3}$$

$$\tilde{H}_2=\bar{\Omega}_{12}^i\Omega_{13}^i/(2\Omega_{23}^i)+\begin{pmatrix}0&0&0\\0&\delta_2^i&0\\0&0&\delta_3^i\end{pmatrix}, \tag{S4}$$

$$\tilde{H}_Z=\begin{pmatrix}0 & -i\frac{\Gamma_{12}^i}{2}e^{-2iy} & 0\\ i\frac{\Gamma_{12}^i}{2}e^{2iy} & 0 & 0\\ 0 & 0 & 0\end{pmatrix}, \tag{S5}$$

with $\delta_2^i=-\left[\bar{\Omega}_{12}^i\Omega_{13}^i/(2\Omega_{23}^i)-\bar{\Omega}_{12}^i\Omega_{23}^i/(2\Omega_{13}^i)\right]+\delta_2$ and $\delta_3^i=-\left[\bar{\Omega}_{12}^i\Omega_{13}^i/(2\Omega_{23}^i)-\Omega_{13}^i\Omega_{23}^i/(2\bar{\Omega}_{12}^i)\right]+\delta_3$.

The eigenstates of atom-light interaction Hamiltonian $\tilde{H}_1$ contain two degenerate dark states $|D_1\rangle$ and $|D_2\rangle$ with the energy $E_{D_1}=E_{D_2}=0$ and one bright state with $E_B=-\frac{1}{2}\left(\frac{\bar{\Omega}_{12}^i\Omega_{13}^i}{\Omega_{23}^i}+\frac{\bar{\Omega}_{12}^i\Omega_{23}^i}{\Omega_{13}^i}+\frac{\Omega_{23}^i\Omega_{13}^i}{\bar{\Omega}_{12}^i}\right)$. The two degenerate

dark states are

$$|D_1^i\rangle = N_1^i\left(-\Omega_{23}^i e^{-iy}|1\rangle + \Omega_{13}^i e^{iy}|2\rangle\right), \tag{S6}$$
$$|D_2^i\rangle = N_2^i\left(\Omega_{13}^i e^{-iy}|1\rangle + \Omega_{23}^i e^{iy}|2\rangle - \Omega_3^i e^{-ix}|3\rangle\right), \tag{S7}$$

where $\Omega_3^i = \bar{\Omega}_{12}^i \frac{\Omega_{13}^{i2}+\Omega_{23}^{i2}}{\Omega_{13}^i\Omega_{23}^i}$, $N_1^i = \frac{1}{\sqrt{\Omega_{23}^{i2}+\Omega_{13}^{i2}}}$, and $N_2^i = \frac{1}{\sqrt{\Omega_{13}^{i2}+\Omega_{23}^{i2}+\Omega_3^{i2}}}$. In the experiment, $\bar{\Omega}_{12}^i < 0$ and $\Omega_{13}^i, \Omega_{23}^i > 0$, therefore $E_B > 0$ and two dark states are the ground states.

We assume that the quantum state of an atom adiabatically stays in the subspace spanned by the two degenerate dark states, thus the state can be written as $|\psi\rangle = \psi_1^i(\mathbf{r},t)|D_1^i\rangle + \psi_2^i(\mathbf{r},t)|D_2^i\rangle$. $\psi(\mathbf{r},t) = [\psi_1^i(\mathbf{r},t), \psi_2^i(\mathbf{r},t)]^T$ satisfies the following equation

$$i\partial_t\psi(\mathbf{r},t) = H_{eff}\psi(\mathbf{r},t), \tag{S8}$$

with the effective 2×2 Hamiltonian

$$H_{eff} = \mathbf{p}^2 + \gamma_y^i p_y + \beta_x^i p_x + (-\alpha_y^i p_y + h_x^i)\sigma_x + \left[\beta_y^i p_y - \beta_x^i p_x + h_z^i\right]\sigma_z + h_\perp^i \sigma_y + \epsilon_0^i.$$

Here $\gamma_y^i = (\Omega_{23}^{i2} - \Omega_{13}^{i2})(N_1^{i2} - N_2^{i2})$, $\beta_x^i = N_2^{i2}\Omega_3^{i2}$, $\alpha_y^i = 4N_1^iN_2^i\Omega_{13}^i\Omega_{23}^i$, $h_x^i = N_1^iN_2^i\Omega_{13}^i\Omega_{23}^i\delta_2^i$, $\beta_y^i = (\Omega_{23}^{i2} - \Omega_{13}^{i2})(N_1^{i2} + N_2^{i2})$, $h_z^i = \left[(N_1^{i2}\Omega_{13}^{i2} - N_2^{i2}\Omega_{23}^{i2})\delta_2^i - N_2^{i2}\Omega_3^{i2}\delta_3^i\right]/2$, $h_\perp^i = -\frac{\Gamma_{12}^i}{2}N_1^iN_2^i(\Omega_{23}^{i2} + \Omega_{13}^{i2}) = -\frac{\Gamma_{12}^i}{2}N_2^i/N_1^i$, $h_0^i = \left[(N_1^{i2}\Omega_{13}^{i2} + N_2^{i2}\Omega_{23}^{i2})\delta_2^i + N_2^{i2}\Omega_3^{i2}\delta_3^i\right]/2$, and $\epsilon_0^i = \bar{\Omega}_{12}^i\Omega_{13}^i/(2\Omega_{23}^i) + h_0^i + 1$.

For case I, $\Gamma_{12}^I = 0$, thus $h_\perp^I = 0$. In this case, the Dirac cone appears at $p_y = h_x^i/\alpha_y^i = \delta_2^i/4$ and $p_x = (h_z^i + \beta_y^i h_x^i/\alpha_y^i)/\beta_x^i = (h_z^i + \beta_y^i\delta_2^i/4)/\beta_x^i$. In case II, $\Gamma_{12}^{II} \neq 0$ and $h_\perp^{II} \neq 0$, a band gap is opened at the Dirac point.

Using the transformation

$$\begin{pmatrix}\psi_1^i\\ \psi_2^i\end{pmatrix} = e^{i(-\gamma_y^i y - \beta_x^i x)/2}e^{-i\pi/4\sigma_x}\begin{pmatrix}\phi_1^i\\ \phi_2^i\end{pmatrix},$$

the effective Hamiltonian (the Eq. (2) in the main text) can be written as

$$H_{eff} = \mathbf{p}^2 + H_{SOC}^i + V_I^i + V_z^i\sigma_z + \tilde{\epsilon}_0^i, \tag{S9}$$

where the 2D SOC $H_{SOC}^i = -\alpha_y^i p_y\sigma_x + \left(\beta_x^i p_x - \beta_y^i p_y\right)\sigma_y$, the in-plane Zeeman field $V_I^i = V_x^i\sigma_x + V_y^i\sigma_y$ with $V_x^i = \alpha_y^i\gamma_y^i/2 + h_x^i$ and $V_y^i = \beta_x^{i2}/2 + \beta_y^i\gamma_y^i/2 - h_z^i$, the perpendicular Zeeman field $V_z^i = h_\perp^i$, and the constant energy shift $\tilde{\epsilon}_0^i = \epsilon_0^i - \beta_x^{i2}/4 - \gamma_y^{i2}/4$. For the specific case that $-\Omega_{12}^i = \Omega_{23}^i = \Omega_{13}^i = \Omega$, $\delta_2 = \delta_3 = 0$, we have $N_1^i = \frac{1}{\sqrt{2}\Omega}$, $N_2^i = \frac{1}{\sqrt{6}\Omega}$, $\alpha_x^i = \frac{2}{\sqrt{3}}$, $\beta_x^i = \frac{2}{3}$, and $h_x^i = h_0^i = h_z^i = \gamma_y^i = \beta_y^i = 0$. The effective Hamiltonian reduces to

$$H_{eff} = \mathbf{p}^2 - \frac{2}{\sqrt{3}}p_y\sigma_x + \frac{2}{3}p_x\sigma_y + \frac{2}{9}\sigma_y + V_z\sigma_z \tag{S10}$$

In case I, $\bar{\Omega}_{12}^I = \Omega_{12}$, $\Omega_{13}^I = \Omega_{13}\cos\theta$, $\Omega_{23}^I = \Omega_{23}\cos\theta$, and $\Gamma_{12}^I = 0$, and there exist a Dirac point. In case II, $\bar{\Omega}_{12}^{II} = \Omega_{12}\cos^2\theta$, $\Omega_{13}^{II} = \Omega_{13}\cos\theta$, $\Omega_{23}^{II} = \Omega_{23}\cos\theta$, and $\Gamma_{12}^{II} = \Omega_{12}\sin^2\theta$, a band gap (Eq. (3) in the main text)

$$\Delta = 2|V_z^{II}| = \sin^2\theta\left[\Omega_{12}^{-2} + \cos^2\theta\left(\Omega_{13}^{-2} + \Omega_{23}^{-2}\right)\right]^{-1/2}. \tag{S11}$$

is opened at the Dirac point

$$\begin{aligned} p_y^{II} &= \frac{\Omega_{12}}{8}\frac{\Omega_{23}^2 - \Omega_{13}^2}{\Omega_{13}\Omega_{23}}\cos^2\theta + \frac{\delta_2}{4} \\ p_x^{II} &= (h_z^{II} + \beta_y^{II}p_y^{II})/\beta_x^{II}. \end{aligned} \tag{S12}$$